



1 **Driven magmatism and crustal thinning of coastal South**
2 **China in response to subduction**

3 Jinbao Su^{1*}, Wenbin Zhu², Guangwei Li²

4 1 College of Oceanography, Hohai University, Nanjing 210098, China

5 2 State Key Laboratory for Mineral Deposits Research, Nanjing University, Nanjing
6 210023, China

7 **Abstract**

8 The late Mesozoic igneous rocks along the coastal South China Block (SCB) exhibit
9 complex parental sources involving a depleted mantle, subducted sediment-derived
10 melt, and melted crust. This period aligns with the magmatic flareup and lull in the SCB,
11 debating with the compression or extension in coastal region. Our study employs
12 numerical models to investigate the dynamics of the ascent of underplating magma
13 along the Changle-Nan'ao Belt (CNB), simulating its intrusion and cooling processes
14 while disregarding the formational background. The rheological structure of the
15 lithospheric mantle significantly influences magma pathways, dictating the distribution
16 of magmatism. This work reveals that the ascent of magma in the presence of faults is
17 considerably faster than that in the absence of faults, and contemporaneous magmatic
18 melts could produce different cooling and diagenetic processes. Additionally, the
19 influence of pre-existing magma accelerates underplating magma emplacement. The
20 ascending of magma forms a mush-like head, contributing to magmatic circulation
21 beneath the crust and decreasing crustal thickness. Multiphase magmatism increases
22 the geothermal gradient, reducing the lithospheric viscosity and promoting
23 underplating magma ascent, leading to magmatic flare-ups and lulls. Our findings
24 suggest that the Cretaceous magmatism at different times in the coastal SCB may be
25 associated with the effects of lithospheric faults under similar subduction conditions.
26 Boundary compression forces delay magma ascent, while rising magma induces a
27 significant circulation, decreasing the crustal thickness of the coastal SCB. This study
28 provides new insights into the complex interplay of magmatic processes during
29 subduction, emphasizing the role of lithospheric structure in shaping the temporal and
30 spatial evolution of coastal magmatism.

¹ * Corresponding authors. E-mail addresses: jin.su@163.com



31 **Keywords**

32 South China; Crustal thinning; Coastal orogeny; Magmatic dynamics; Three-phase
33 flow

34 **1 Introduction**

35 Magmatism characterized by periodic flare-ups and lulls at convergent plate margins
36 usually manifests a subduction-related origin (Brown, 1994). However, there is no an
37 agreement regarding the relationships between magmatism and the roles of subducted
38 slabs and the corresponding subduction styles (Morris et al., 2000; Faccenna et al.,
39 2010). Instead, a contradictory and multifaceted dynamic process emerges due to the
40 complex magmatic composition (Yoo and Lee, 2023). In the eastern region of the South
41 China Block (SCB), tectonic magmatism spanned a considerable time span during the
42 Mesozoic (Zhou et al., 2006). Notably, the absence of high-pressure blueschist, which
43 is typically associated with subduction, has generated intense debate surrounding the
44 accurate timing of initial subduction and variations in slab dip, with proposals ranging
45 from flat-slab subduction to shallow and steep subduction (Suo et al., 2019; Xu, 2023;
46 Su, 2023). Some researchers proposed a model involving early Permian flat-slab
47 subduction and Jurassic foundering model in the SCB; however, this model lacks
48 substantial evidence of early-stage subduction-related magma (Li and Li, 2007). While
49 most research has focused on Jurassic subduction, early Jurassic intraplate igneous
50 rocks deviate from typical subduction arc-related rocks and display inconsistencies in
51 spatiotemporal distribution during coastward migration (Zhou and Li, 2000; Xu et al.,
52 2017; Li et al., 2019). Researchers contend that the SCB did not immediately
53 experience the influence of the Paleo-Pacific Plate in the Early–Middle Jurassic but
54 experienced intensified activity in the Late Jurassic to Cretaceous (Gan et al., 2021).
55 Gradual steepening of the shallowly subducting slab since the Middle Jurassic is
56 proposed to explain the corresponding flare-up of magmatism in the SCB (Zhou et al.,
57 2006; Mao et al., 2021). In contrast, Xu et al. (2023) interpreted voluminous intraplate
58 silicic magmatism as a response to slab stagnation and coastward migration,
59 overlooking contemporaneous compressional deformation in the Late Jurassic and
60 early–middle Cretaceous. In contrast to the coastward migration model, the early–
61 middle Cretaceous is considered a magmatic lull resulting from crustal shortening due
62 to resubduction of the slab (Wei et al., 2023). The uncertainty lies in whether
63 subduction-induced magma can migrate and intrude concurrently according to these



64 different models. The Mesozoic tectonic magmatism in the SCB was intricately linked
65 not only to the lithospheric properties but also to subduction rates and mantle flow (Su,
66 2023). The transport of intrusive magma spans a significant period, and the pathways
67 of ascending magma play a crucial role in determining the distribution of magmatism
68 during the emplacement process. Unfortunately, lag magma, which is potentially
69 misunderstood as originating from other sources, has received limited attention in
70 current discussions.

71 The coastal South China Block (SCB) is characterized by the development of a 40-
72 60 km wide NE–SW striking ductile shear zone known as the Changle-Nan’ao Belt
73 (CNB) (Cui et al., 2013). This belt comprises gneiss exhibiting evidence of
74 metamorphism at greenschist, amphibolite, and granulite facies (Li et al., 2015).
75 Intrusions of gabbro, diorite, granodiorite, monzogranite, and two-mica granite plutons
76 are also prevalent within the CNB. The U–Pb age analysis of the oldest orthogneiss in
77 the CNB yields a date of 187 ± 1 Ma, with the youngest orthogneiss dating to 130 ± 1
78 Ma. Additionally, $^{40}\text{Ar}/^{39}\text{Ar}$ plateau ages fall within the range of 118–107 Ma (Wang
79 and Lu, 2000). The occurrence of voluminous igneous rocks spans two significant
80 periods, ranging from 143–130 Ma and 110–95 Ma. A debated magmatic lull observed
81 between 130 and 110 Ma is associated with syncollisional orogenesis (Chen et al., 2020;
82 Wei et al., 2023) or postorogenic extension (Cui et al., 2013; Li et al., 2014; Zhao et al.,
83 2015; Xu et al., 2023) according to the involved deformation and magmatic rocks.
84 Despite these insights, the relationship between intruded magma and orogenesis
85 remains uncertain, mirroring the ambiguous understanding of potential variations in
86 magma migration time in response to tectonic stress. In addressing this uncertainty, our
87 exploration focuses on understanding the emplacement and cooling process of mantle
88 magmatism and its influence on crustal structure. Additionally, we delve into the
89 question of whether changes in the dynamic background instantaneously produce
90 magmas with different properties that can effectively intrude shallow layers.

91 **2 Emplacement and origin of Cretaceous magma**

92 Cretaceous magmatic rocks cover an area of approximately 117,190 km² on the
93 southeastern coast and in the Lower Yangtze region of the SCB (Liu et al., 2020). The
94 crustal Poisson’s ratios range from 0.22–0.26 in the interior to 0.26–0.29 in the eastern
95 coastal region, implying a high content of felsic minerals and an increasing proportion
96 of mafic minerals from the interior to the coast (Guo et al., 2019). Seismic profiles



97 reveal transparent reflective features of felsic rocks in the upper crust and abundant
98 high-amplitude, short isolated reflections of mafic sills in the mid-lower crust (Li et al.,
99 2023). The velocity's ratio of P waves and S waves (V_p/V_s) on the coast is 1.76, which
100 is slightly greater than that in the interior SCB but lower than the value of 1.79 for mafic
101 underplating of the lower crust (Deng et al., 2019). The coastal V_p values of the lower
102 crust (~ 6.5 km/s) are not compatible with the mafic composition ($V_p > 7.0$ km/s),
103 implying that mafic magma underplating was not common or was removed (Guo et al.,
104 2019). However, high resistive anomalies in electrical resistivity profiles indicate local
105 mafic magma underplating (Cheng et al., 2021).

106 The coastal granitic gneisses exhibit varying cooling rates during different periods.
107 These rates were $\sim 35^\circ\text{C}/\text{Myr}$ at 130–120 Ma, $13\text{--}20^\circ\text{C}/\text{Myr}$ at 126–110 Ma, $\sim 10^\circ\text{C}/\text{Myr}$
108 at 110–100 Ma, and $\sim 80^\circ\text{C}/\text{Myr}$ at 100–90 Ma (Chen et al., 2002, 2020). The structural
109 pattern of the CNB shows solid-state ductile deformation with temperatures of 300–
110 350°C in the mylonitic gneiss and deformed volcanic rocks. Syntectonic granitoids
111 exhibit subsolidus magmatic flow (Wang and Lu, 2000; Wei et al., 2015). The
112 temperature and pressure of metamorphic minerals are $540\text{--}610^\circ\text{C}$ and 0.28–0.35 GPa,
113 respectively, based on plagioclase-amphibolite, and $485\text{--}640^\circ\text{C}$ and 0.3 GPa,
114 respectively, based on a mica-quartz schist (Wang and Lu, 2000). The Cretaceous
115 magmatic rocks in the SCB belong to the I-and A-type series, with high-K calc-alkaline
116 to shoshonitic affinities and arc-like features. They are enriched in light rare earth
117 elements (LREEs) and large ion lithophile elements (LILEs) but depleted in heavy rare
118 earth elements (HREEs) and high field strength elements (HFSEs). They exhibit
119 negative $\epsilon\text{Nd}(t)$ values ranging from -10.1 to -0.3 , and variable zircon $\epsilon\text{Hf}(t)$ values
120 ranging from -29.7 to $+10.3$. The mafic rocks have $\epsilon\text{Nd}(t)$ values ranging from -14.27
121 to $+8.0$, and $\epsilon\text{Hf}(t)$ values ranging from -9.5 to $+1.9$ (Chen et al., 2020). Isotopic data
122 indicate mixed sources, including ancient crust-derived, enriched mantle-derived and
123 depleted mantle-derived material. Some mafic rocks possibly originated from the
124 melting of the mantle wedge metasomatized by melts from the subducted slab and
125 sediments.

126 The mixed magmatic source indicates that partial melting was independent of the
127 type of subduction transport across the lithosphere. Subduction-induced melts migrate
128 upward, and their pathways change depending on the stress conditions, resulting in
129 different time–temperature histories for emplacement and deformation of gneissic



130 magma.

131 **3 Numerical simulation and model setup**

132 The Late Mesozoic Magmatism of the SCB was triggered by the subduction of the
133 Paleo-Pacific plate (Su, 2023). A substantial volume of magma, originating from the
134 subducted slab, asthenosphere, and the lithospheric base, ascended towards the surface and
135 accumulated at the lower boundary of the lithosphere (Fig. 2a). To unravel the dynamics
136 of coastal magmatism in response to subduction geometry, two end-member numerical
137 models are considered. Our simulation focuses solely on modeling the intrusion and ascent
138 of magma that has accumulated at the bottom of the lithosphere, without delving into the
139 origins of magma from deeper sources (Fig. 2b). The models are two-dimensional
140 domains with 400 km wide and 100 km deep, representing a trench-perpendicular
141 cross-section of a subduction zone with the trench located to the right of the model. The
142 underplating magma is represented by a 4-8 km thick body located at 100-80 km depth
143 along the bottom of the model. The 8 km-thick magma represents the accumulation of
144 underplating magma due to the subduction. A 10 km thick square domain is assigned at
145 40 km depth, representing previously intruded magma in the lithospheric mantle. The
146 upper 30 km deep rectangle is continental crust. The polygon located between the
147 underplating magma and crust is mantle lithosphere. A 4 km wide rectangular domain
148 is assigned at the left of the model representing a lithospheric fault.

149 *3.1 Governing equations*

150 The materials of the domain are regarded as incompressible viscous fluids according
151 to the Boussinesq approximation. The models satisfy the following mass, momentum,
152 and energy conservation equations:

$$153 \quad \nabla u = 0 \quad (1)$$

$$154 \quad \nabla \cdot [\eta \cdot (\nabla u + (\nabla u)^T)] - \nabla P + \rho g = 0 \quad (2)$$

$$155 \quad \rho C_p \cdot \left(\frac{\partial T}{\partial t} + u \nabla T \right) = \nabla (k \nabla T) - \alpha \rho v_z T \quad (3)$$

156 where u is the velocity field, η is the viscosity, T is the temperature, P is the
157 pressure, ρ is the density, g is gravity, C_p is the specific heat, t is the time, k is the
158 thermal conductivity, α is the thermal expansion coefficient and v_z is the vertical
159 velocity component (Rodríguez-González et al., 2012). The heat capacity is set to 1000
160 J/(kg·K), the ratio of specific heat (γ) is set to 1 and the thermal conductivity is
161 set at 2.5 W/(m·K) in all domains of models (Chapman, 2021). The density of the
162 continental crust varies linearly with depth, increasing from 2600 kg/m³ at the surface



163 to 2900 kg/m³ at 30 km depth. The mantle lithosphere has a constant density of 3400
164 kg/m³, whereas the molten magma is modeled with a constant density of 2800 kg/m³.

165 The crustal material has power-law stress-strain rate relationship (Chapman, 2021).

166 η is the dynamic viscosity and its expression is:

$$167 \quad \eta = \frac{n}{\sqrt{A f_{H_2O}}} \frac{dP}{\epsilon_{II}^{1-n/n}} \times \exp\left(\frac{E + P_{lit} \times V}{n \times R \times T}\right) \quad (4)$$

168 where A is the pre-exponential factor; E and V are the activation energy and volume,
169 respectively; P_{lit} is the lithostatic pressure; R is the gas constant; and n is the stress
170 exponent. The dynamic viscosity was calculated using the wet quartz flow law of
171 Hirth et al. (2001). The viscosity was calculated at each time step using the
172 temperatures returned from the model, a quartz material parameter (A) of 1.36742x10⁻⁵
173 MPa⁻ⁿ/s with a stress exponent (n) of 4, a quartz activation energy (E) of 135 kJ/mol,
174 a water fugacity (f_{H_2O}) of 1,000 MPa, and a strain rate of 10⁻¹⁵ s⁻¹ (Chapman, 2021).
175 The strain applied in the modeling is taking a 2D approximation and is based on slab
176 subduction studies (Liu and Currie, 2019). The viscosity was updated after each time
177 step based on the temperature. The mantle lithosphere and the molten magma are
178 modeled with a constant dynamic viscosity of 1e21 Pa·s and 1e20 Pa·s, respectively.
179 The heat capacity is set to 1000 J/(kg·K), the ratio of specific heat (γ) is set to 1
180 and the thermal conductivity is set at 2.5 W/(m·K) in all domains of models
181 (Chapman, 2021).

182 The models are run using the three-phase flow, phase field interface option, which
183 accounts for the surface tension between immiscible phases, the contact angles with
184 the walls, and the density and viscosity of each fluid. The three-phase flow model
185 obeys Cahn-Hilliard equation (Boyer et al., 2010). The fluid motion causes the phase
186 field variable to change from phase to phase, but the sum of all phase field variables ϕ_i
187 at each point in the space is 1. Its expression consists of the order parameter of each phase
188 as in equation

$$189 \quad \begin{cases} \phi_i = \phi_i \\ \phi_a + \phi_b + \phi_c = 1 \end{cases} \quad (5)$$

190 The three phases are continental crust ϕ_a , mantle lithosphere ϕ_b and magma ϕ_c . Three
191 phase flow is automatically computed using a Phase Initialization study step by solving
192 for the geometrical distance to the initial interface. The initialized three phase flow



193 function is then defined from the analytical steady state solution for a straight fluid-fluid
194 interface.

195 *3.2 Model setup*

196 The resolution of model is physically controlled, but generally represented by a
197 triangular mesh with side lengths of 2-5 km. The top and sides of the model are no-
198 slip boundaries and are fixed, whereas the bottom of the model is a free-slip
199 boundary. Model 2 is assigned a $1e9$ Pa boundary force on the right side, representing
200 the compression effect induced by subduction. The sides of the model are thermally
201 insulated and the top and bottom are held at constant temperature of 0°C and 950°C ,
202 respectively. The initial temperature of the underplating magma is 1250°C . The
203 geothermal gradient was assumed to be $3^{\circ}\text{C}/100\text{m}$.

204 In Model 1, magma underplating at varying depths and a lithospheric fault are
205 included to simulate the ascent of magma originating from subduction. In contrast,
206 Model 2 includes a boundary force to simulate magmatism influenced by compression
207 during subduction. The numerical experiments were conducted utilizing the finite-
208 element software COMSOL Multiphysics, accessible at <https://www.comsol.com>. The
209 lithospheric thickness was estimated based on the current thickness derived from P-
210 wave velocity measurements (Deng et al., 2019). The density and viscosity of magma
211 were coupled to the thermal model and allowed to vary according to the wet quartz flow
212 law.

213 **4 Underplating magma and circulation**

214 The modeling results elucidated the temporal evolution and migration pathway of
215 magmatism originating from the subsurface. In Model 1 (Fig. 3a-e), underplating
216 magma accumulates at the lithospheric fault and locations of initial thickened magma
217 along the bottom. The magma rises upward, generating mush-like features in the mantle,
218 and grows laterally beneath the location of initial thickened and shallowly assigned
219 magma (Fig. 3). The ascent of magma follows an up-and-down circulation pattern,
220 driving lower crustal thickening and subsidence in front of the growing magma mush.
221 The underplating magma ascends rapidly from the bottom to the lower crust, crossing
222 a distance of approximately 80 km within 20 Myr through the lithospheric fault (Fig.
223 3), whereas, without a fault, the magma ascends a distance of only 60 km. In Model 2
224 (Fig. 3f-j), under the influence of compression from the right boundary, the diapiric
225 magma exhibits slight migration to the left, causing thinning of the crust to the right.



226 The migration of magma and the temporal pattern are significantly influenced by
227 lithospheric viscosity and temperature (Chapman, 2021). In our models, we specifically
228 examine the effects of pre-existing magma and a lithospheric fault. The models provide
229 cooling histories for five diapiric underplating magmas, which are then compared with
230 observed coastal magmatism (Fig. 4a). The results indicate a more rapid cooling rate
231 for the ascending magma through the fault ($\sim 35^{\circ}\text{C}/\text{Myr}$) and a slower cooling rate for
232 underplating magma without pre-existing magma. The cooling history of other magmas
233 is inconsistent with that of the actual igneous rocks, emphasizing the influence of the
234 faults in this region. Moreover, the ascent of magma to the location of pre-existing
235 magma is also faster in the absence of a fault (e.g., magma 3, Fig. 3b).

236

237 **5 Discussion and Conclusions**

238 The late Mesozoic igneous rocks along the coastal South China Block (SCB) exhibit
239 a distinctive trend of increasing $\epsilon\text{Hf}(t)$ values, with negative values transitioning to
240 positive values during 110-125 Ma (Fig. 4b). These values suggest these rocks were
241 derived from depleted mantle, subducted sediment-derived melt, and melting crust
242 (Zhao et al., 2015). This period corresponds to the magmatic lull in the SCB and a
243 period of compression in the CNB during 130-105 Ma (Wei et al., 2023). Previous
244 researchers attributed this phase to a transitional stage in subduction status involving
245 slab foundering, break-off, or steepening (Xu et al., 2023). Intriguingly, they
246 demonstrate the potential for producing underplating magma beneath the lithospheric
247 mantle, resulting in different compositions rising into the crust. Therefore, our models
248 adopt underplating magma to simulate its upward magmatic intrusion and cooling
249 processes, irrespective of the formational background. The rheological structure
250 inevitably influences the pathway of underplating magma as it traverses the thick
251 lithospheric mantle, ultimately dictating the distribution of widespread magmatism (Fig.
252 3). High viscosities in the lithospheric mantle may limit magma transport, with the
253 effective viscosity of the upper mantle estimated at approximately $1\text{e}20\text{-}1\text{e}22$ Pa·s in
254 continental China (Shi and Cao, 2008), which decreases with increasing temperature.
255 Considering the widespread magmatism and geothermal activity in the coastal SCB in
256 the Cretaceous, an effective viscosity of $1\text{e}21$ Pa·s for the lithospheric mantle is
257 plausible. The lower viscosity of the CNB compared to that of the interior SCB
258 facilitated the emplacement of mantle magma during the magmatic lull.



259 The rise of underplating magma into the middle crust, an ascent of 80 km, takes 10-
260 20 Myr through a lower-viscosity lithospheric fault, while it takes more than 40 Myr
261 without a fault. This time discrepancy aligns with the magmatic lull in the coastal SCB.
262 Thus, magmatism with different ages in the Cretaceous coastal SCB potentially formed
263 through exploitation of distinct ascent pathways under the same subduction conditions,
264 rather than contemporaneously varying with steepening subduction geometry. Partially
265 molten magma can persist for at least 25 Myr with at temperatures exceeding 700°C
266 (Cavalcante et al., 2018), contributing to the heterogeneous and mixed magmatism
267 observed in the coastal SCB.

268 The ascent of magma generates a mush-like head, accommodating the rheological
269 structure of the lithospheric mantle and leading to magmatic circulation. These magmas
270 underplate beneath the crust, decreasing the crustal thickness at the head and causing
271 crustal subsidence on both sides. Importantly, pre-existing magma can accelerate the
272 emplacement of underplating magma (Fig. 3). The underplating magma beneath the
273 lithospheric mantle ascends rapidly when pre-existing magma is present. It is possible
274 that multiphase magmatism increases the geothermal gradient in the SCB, reducing
275 lithospheric viscosity and further promoting the ascent of underplating magma and the
276 occurrence of a subsequent magmatic flare-up. In addition, the ascent pathways of
277 magma change under the influence of a boundary force, resulting in increased transport
278 time and delayed magmatic emplacement into the crust (Fig. 4c). Continued
279 compression also contributes to the uplift of the lithospheric mantle, which is associated
280 with the removal of crust, thereby decreasing the crustal thickness (Fig. 4c). This
281 provides a new perspective on the crustal thinning of the coastal regions during
282 subduction. The model might oversimplify the complex geological features, potentially
283 leading to inaccurate results. Also, assuming a uniform crustal thickness may not capture
284 the true variability of the crust. The geometry of lithospheric faults in the model is
285 simplified, neglecting important details that could affect magmatic processes

286 The model results describe the pathways and time spans of underplating magma
287 rising into the crust under the influence of a lithospheric fault, pre-existing magma, and
288 boundary stress. Magmatic flare-ups or lulls are not controlled solely by the slab
289 subduction conditions. The Cretaceous magmatism along the coastal SCB could have
290 occurred under the same subduction conditions, with the CNB facilitating the upwelling
291 and intrusion of underplating magma under various regional stresses. A boundary force



292 delays the ascent of underplating magma, while rising magma induces a significant
293 circulation, which would have decreased the crustal thickness of the coastal SCB.

294

295 **6 Acknowledgments**

296 This work was supported by grants from the National Key R&D Program of
297 China (2022YFF0800403) and the Natural Science Foundation of China (42272236)

298

299 **Competing Interest**

300 The authors declare that there is not conflict of interest regarding the publication of
301 this article.

302 **Data availability**

303 The data used in this study are available in the references and Supplementary
304 Material. The finite-element software COMSOL Multiphysics is accessible at
305 <https://www.comsol.com>.

306

307

308

309

310

311 **References**

312 Boyer, F., Lapuerta, C., Minjeaud, S., Piar, B., and Quintard, M.: Cahn-
313 Hilliard/Navier-Stokes model for the simulation of three-phase flows, *Transp. Porous*
314 *Media*, 82, 463–483, <https://doi.org/10.1007/s11242-009-9408-z>, 2010.

315 Brown, M.: The generation, segregation, ascent and emplacement of granite magma:
316 the migmatite-to-crustally-derived granite connection in thickened orogens, *Earth Sci.*
317 *Rev.*, 36, 83–130, [https://doi.org/10.1016/0012-8252\(94\)90009-4](https://doi.org/10.1016/0012-8252(94)90009-4), 1994.

318 Cavalcante, C., Hollanda, M. H., Vauchez, A., and Kawata, M.: How long can the
319 middle crust remain partially molten during orogeny?, *Geology*, 46, 839–842,
320 <https://doi.org/10.1130/G45126.1>, 2018.

321 Chapman, J. B.: Diapiric relamination of the Orocopia Schist (southwestern U.S.)
322 during low-angle subduction, *Geology*, 49, 983–987,
323 <https://doi.org/10.1130/G48647.1>, 2021.

324 Chen, C. H., Lee, C. Y., Tien, J. L., Xiang, H., Walia, M., and Lin, J. W.: Post-



325 orogenic thermal reset of the Pingtan-Dongshan metamorphic belt (SE China):
326 Insights from zircon fission track and U-Pb double dating, *J. Asian Earth Sci.*, 201,
327 104512, <https://doi.org/10.1016/j.jseaes.2020.104512>, 2020.
328 Chen, W. S., Yang, H. C., Wang, X., and Huang, H.: Tectonic setting and exhumation
329 history of the Pingtan-Dongshan Metamorphic Belt along the coastal area, Fujian
330 Province, Southeast China, *J. Asian Earth Sci.*, 20, 829–840,
331 [https://doi.org/10.1016/S1367-9120\(01\)00066-9](https://doi.org/10.1016/S1367-9120(01)00066-9), 2002.
332 Cheng, Y., Han, B., Li, Y., Guo, J., and Hu, X.: Lithospheric electrical structure
333 beneath the Cathaysia Block in South China and its tectonic implications,
334 *Tectonophysics*, 814, 228981, <https://doi.org/10.1016/j.tecto.2021.228981>, 2021.
335 Cui, J., Zhang, Y., Dong, S., Jahn, B. ming, Xu, X., and Ma, L.: Zircon U-Pb
336 geochronology of the Mesozoic metamorphic rocks and granitoids in the coastal
337 tectonic zone of SE China: Constraints on the timing of Late Mesozoic orogeny, *J.*
338 *Asian Earth Sci.*, 62, 237–252, <https://doi.org/10.1016/j.jseaes.2012.09.014>, 2013.
339 Deng, Y., Li, J., Peng, T., Ma, Q., Song, X., Sun, X., Shen, Y., and Fan, W.:
340 Lithospheric structure in the Cathaysia block (South China) and its implication for the
341 Late Mesozoic magmatism, *Phys. Earth Planet. Inter.*, 291, 24–34,
342 <https://doi.org/10.1016/j.pepi.2019.04.003>, 2019.
343 Faccenna, C., Becker, T. W., Lallemand, S., Lagabrielle, Y., Funiciello, F., and
344 Piromallo, C.: Subduction-triggered magmatic pulses: A new class of plumes?, *Earth*
345 *Planet. Sci. Lett.*, 299, 54–68, <https://doi.org/10.1016/j.epsl.2010.08.012>, 2010.
346 Gan, C., Zhang, Y., Wang, Y., Qian, X., and Wang, Y.: Reappraisal of the Mesozoic
347 tectonic transition from the Paleo-Tethyan to Paleo-Pacific domains in South China,
348 *Bull. Geol. Soc. Am.*, 133, 2582–2590, <https://doi.org/10.1130/B35755.1>, 2021.
349 Guo, L., Gao, R., Shi, L., Huang, Z., and Ma, Y.: Crustal thickness and Poisson's
350 ratios of South China revealed from joint inversion of receiver function and gravity
351 data, *Earth Planet. Sci. Lett.*, 510, 142–152,
352 <https://doi.org/10.1016/j.epsl.2018.12.039>, 2019.
353 Li, J., Dong, S., Cawood, P. A., Thybo, H., Clift, P. D., Johnston, S. T., Zhao, G., and
354 Zhang, Y.: Cretaceous long-distance lithospheric extension and surface response in
355 South China, *Earth-Science Rev.*, 243, 104496,
356 <https://doi.org/10.1016/j.earscirev.2023.104496>, 2023.
357 Li, S., Suo, Y., Li, X., Zhou, J., Santosh, M., Wang, P., Wang, G., Guo, L., Yu, S.,



- 358 Lan, H., Dai, L., Zhou, Z., Cao, X., Zhu, J., Liu, B., Jiang, S., Wang, G., and Zhang,
359 G.: Mesozoic tectono-magmatic response in the East Asian ocean-continent
360 connection zone to subduction of the Paleo-Pacific Plate, *Earth-Science Rev.*, 192,
361 91–137, <https://doi.org/10.1016/j.earscirev.2019.03.003>, 2019.
- 362 Li, Y., Ma, C. Q., Xing, G. F., and Zhou, H. W.: The Early Cretaceous evolution of
363 SE China: Insights from the Changle-Nan’ao Metamorphic Belt, *Lithos*, 230, 94–104,
364 <https://doi.org/10.1016/j.lithos.2015.05.014>, 2015.
- 365 Li, Z.-X. and Li, X.-H.: Formation of the 1300-km-wide intracontinental orogen and
366 postorogenic magmatic province in Mesozoic South China: a flat-slab subduction
367 model, *Geology*, 35, 179–182, 2007.
- 368 Li, Z., Qiu, J. S., and Yang, X. M.: A review of the geochronology and geochemistry
369 of Late Yanshanian (Cretaceous) plutons along the Fujian coastal area of southeastern
370 China: Implications for magma evolution related to slab break-off and rollback in the
371 Cretaceous, *Earth-Science Rev.*, 128, 232–248,
372 <https://doi.org/10.1016/j.earscirev.2013.09.007>, 2014.
- 373 Liu, J. X., Wang, S., Wang, X. L., Du, D. H., Xing, G. F., Fu, J. M., Chen, X., and
374 Sun, Z. M.: Refining the spatio-temporal distributions of Mesozoic granitoids and
375 volcanic rocks in SE China, *J. Asian Earth Sci.*, 201, 104503,
376 <https://doi.org/10.1016/j.jseaes.2020.104503>, 2020.
- 377 Mao, J., Zheng, W., Xie, G., Lehmann, B., and Goldfarb, R.: Recognition of a
378 Middle–Late Jurassic arc-related porphyry copper belt along the southeast China
379 coast: Geological characteristics and metallogenic implications, *Geology*, XX, 1–5,
380 <https://doi.org/10.1130/g48615.1>, 2021.
- 381 Morris, G., Larson, P. B., and Hooper, P. R.: ‘Subduction Style’ Magmatism in a Non-
382 subduction Setting: the Colville Igneous Complex, NE Washington State, USA, *J.*
383 *Petrol.*, 41, 43–67, 2000.
- 384 Rodríguez-González, J., Negredo, A. M., and Billen, M. I.: The role of the overriding
385 plate thermal state on slab dip variability and on the occurrence of flat subduction,
386 *Geochemistry, Geophys. Geosystems*, 13, 1–21,
387 <https://doi.org/10.1029/2011GC003859>, 2012.
- 388 Shi, Y. and Cao, J.: Lithosphere Effective Viscosity of Continental China, *Earth Sci.*
389 *Front.*, 15, 82–95, [https://doi.org/10.1016/s1872-5791\(08\)60064-0](https://doi.org/10.1016/s1872-5791(08)60064-0), 2008.
- 390 Su, J.: Accelerated subduction of the western Pacific Plate promotes the



391 intracontinental uplift and magmatism in late Jurassic South China, *Tectonophysics*,
392 869, 230136, <https://doi.org/10.1016/j.tecto.2023.230136>, 2023.

393 Suo, Y., Li, S., Jin, C., Zhang, Y., Zhou, J., Li, X., Wang, P., Liu, Z., Wang, X., and
394 Somerville, I.: Eastward tectonic migration and transition of the Jurassic-Cretaceous
395 Andean-type continental margin along Southeast China, *Earth-Science Rev.*, 102884,
396 2019.

397 Wang, Z. H. and Lu, H. F.: Ductile deformation and $^{40}\text{Ar}/^{39}\text{Ar}$ dating of the
398 Changle-Nanao ductile shear zone, southeastern China, *J. Struct. Geol.*, 22, 561–570,
399 [https://doi.org/10.1016/S0191-8141\(99\)00179-0](https://doi.org/10.1016/S0191-8141(99)00179-0), 2000.

400 Wei, W., Faure, M., Chen, Y., Ji, W., Lin, W., Wang, Q., Yan, Q., and Hou, Q.:
401 Back-thrusting response of continental collision: Early Cretaceous NW-directed
402 thrusting in the Changle-Nan’ao belt (Southeast China), *J. Asian Earth Sci.*, 100, 98–
403 114, <https://doi.org/10.1016/j.jseaes.2015.01.005>, 2015.

404 Wei, W., Lin, W., Chen, Y., Faure, M., Ji, W., Hou, Q., Yan, Q., and Wang, Q.:
405 Tectonic Controls on Magmatic Tempo in an Active Continental Margin: Insights
406 From the Early Cretaceous Syn-Tectonic Magmatism in the Changle-Nan’ao Belt,
407 South China, *J. Geophys. Res. Solid Earth*, 128,
408 <https://doi.org/10.1029/2022JB025973>, 2023.

409 Xu, C., Zhang, L., Shi, H., Brix, M. R., Huhma, H., Chen, L., Zhang, M., and Zhou,
410 Z.: Tracing an Early Jurassic magmatic arc from South to East China Seas, *Tectonics*,
411 36, 466–492, <https://doi.org/10.1002/2016TC004446>, 2017.

412 Xu, C., Deng, Y., Barnes, C. G., Shi, H., Pascal, C., Li, Y., Gao, S., Jiang, D., Xie, J.,
413 and Ma, C.: Offshore-onshore tectonomagmatic correlations: Towards a Late
414 Mesozoic non-Andean-type Cathaysian continental margin, *Earth-Science Rev.*, 240,
415 104382, <https://doi.org/10.1016/j.earscirev.2023.104382>, 2023.

416 Xu, X.: Late Triassic to Middle Jurassic tectonic evolution of the South China Block:
417 Geodynamic transition from the Paleo-Tethys to the Paleo-Pacific regimes, *Earth-*
418 *Science Rev.*, 241, 104404, <https://doi.org/10.1016/j.earscirev.2023.104404>, 2023.

419 Yoo, S. and Lee, C.: Controls on melt focusing beneath old subduction zones: A case
420 study of northeast Japan, *Tectonophysics*, 851, 229766,
421 <https://doi.org/10.1016/j.tecto.2023.229766>, 2023.

422 Zhao, J. L., Qiu, J. S., Liu, L., and Wang, R. Q.: Geochronological, geochemical and
423 Nd-Hf isotopic constraints on the petrogenesis of Late Cretaceous A-type granites



424 from the southeastern coast of Fujian Province, South China, *J. Asian Earth Sci.*, 105,
425 338–359, <https://doi.org/10.1016/j.jseaes.2015.01.022>, 2015.

426 Zhou, X., Sun, T., Shen, W., Shu, L., and Niu, Y.: Petrogenesis of Mesozoic
427 granitoids and volcanic rocks in South China: a response to tectonic evolution,
428 *Episodes*, 29, 26–33, 2006.

429 Zhou, X. M. and Li, W. X.: Origin of Late Mesozoic igneous rocks in Southeastern
430 China: implications for lithosphere subduction and underplating of mafic magmas,
431 *Tectonophysics*, 326, 269–287, 2000.

432

433

434

435

436

437

438

439

440

441

442

443

444

445

446

447

448

449

450

451

452

453

454

455

456



457 **Figure captions**

458 Fig. 1 (A) Regional geological map of Southeast China showing distribution of
459 Mesozoic magma; (B) geological magmatism of the Changle-Nan'ao Belt and
460 corresponding ages (Refer to Wei et al. 2023).

461

462 Fig. 2 (A) Schematic cross section illustrating the subduction of the Paleo-Pacific plate.
463 (B) Reference model geometry depicting temperature, density and viscosity variations
464 with depth.

465

466 Fig. 3 Results of Models 1 and 2, illustrating magma upwelling for 1-5 myr, respectively.
467 (a)-(e): Model 1; (f)-(j): Model 2 with compression on the right side.

468

469 Fig. 4 (A) Zircon Hf isotopes and ages of coastal magmatic rocks in the SCB (data from
470 Li et al., 2023). (b) Comparison of the observed cooling histories of CNB magmatic
471 plutons (data from Chen et al. 2020) with time–temperature paths generated by models
472 of rising magma. (c) Sketch illustrating the formation stage of the underplating magma
473 and tectonic background during 80-110 Ma, 110-130 Ma and 130-160 Ma, respectively.

474

475

476

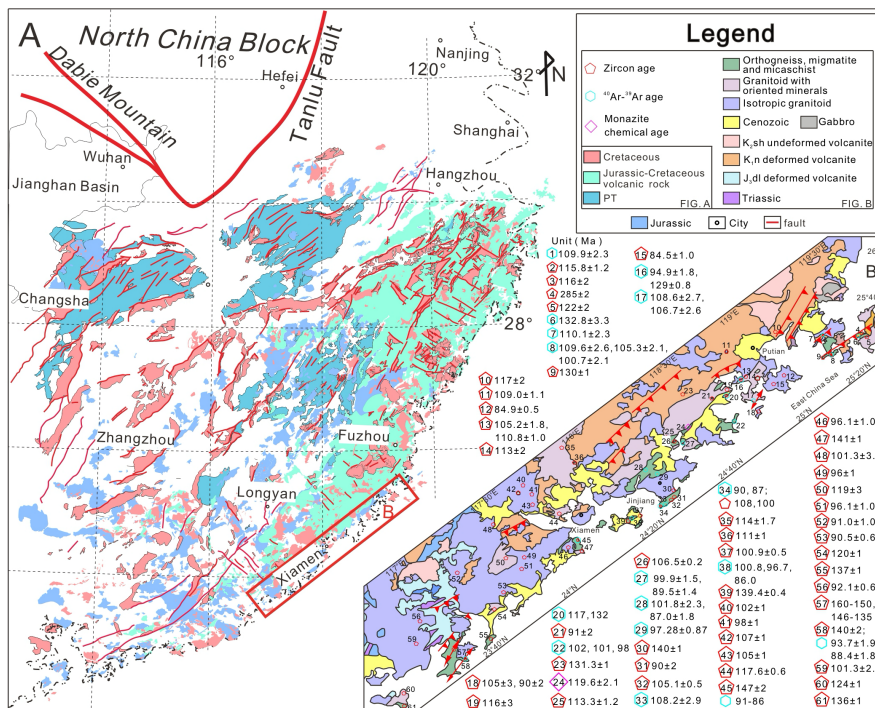


Fig 1

477
478
479
480

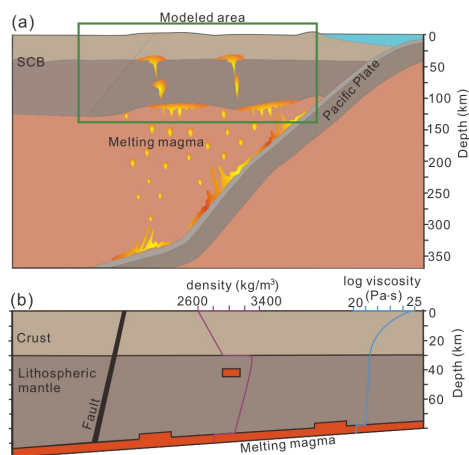


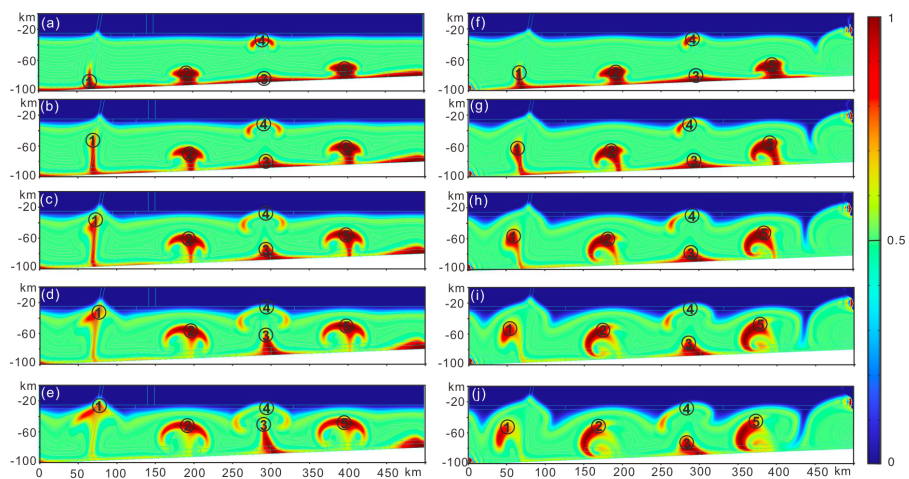
Fig. 2

481
482
483
484
485



486

487



488

489

490

Fig. 3

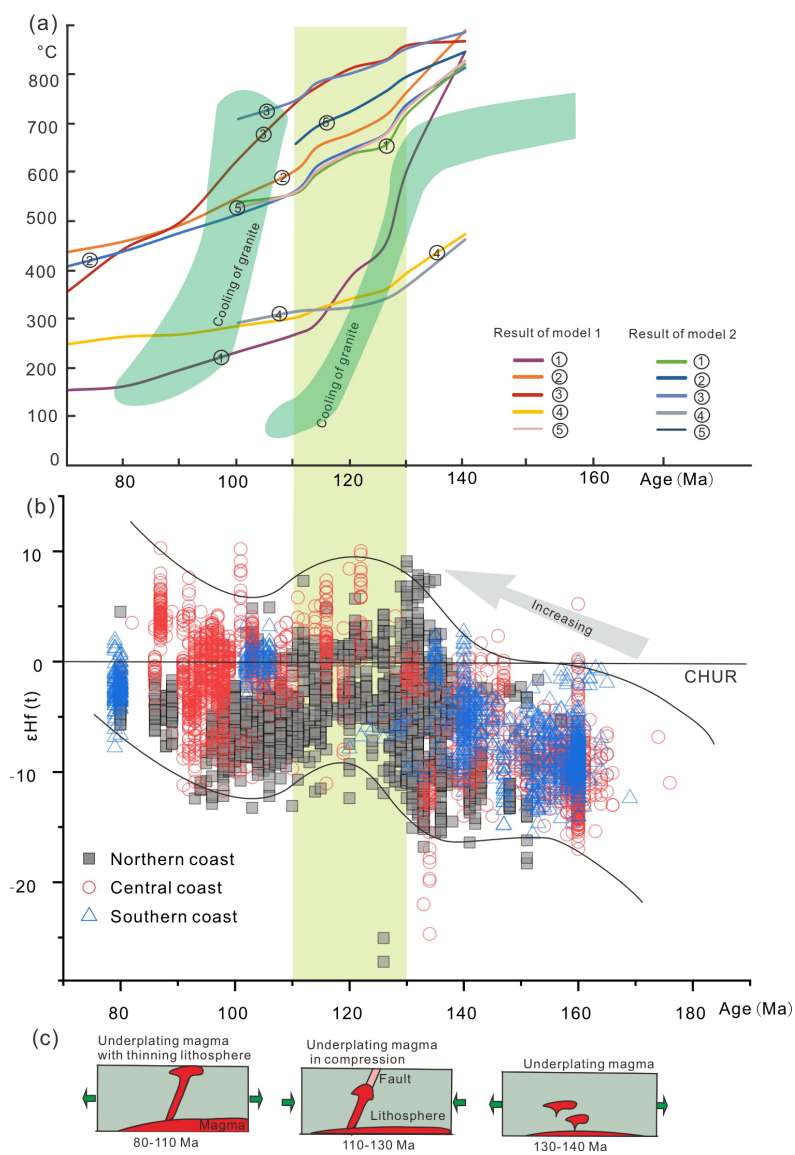


Fig. 4

491
492
493
494
495